Delta and Inverse Delta Coupler Optimization Using Machine Learning for Wireless Power Transfer Electric Vehicle Charging Application

Rahulkumar J and Narayanamoorthi R, *Member, IEEE*

***Abstract*—A wireless resonant inductive power transfer (WRIPT)-based electric vehicle charging system requires an efficient lightweight inductive coupler with high misalignment tolerance. This article proposes a new delta and inverse delta (Δ–∇) coil geometry coupler and a machine learning (ML)-based reinforcement algorithm for Δ–∇ coupler optimization. Δ–∇ is a combination of Δ and ∇ geometry coils, which introduce a diagonal flux pipe compared with the conventional geometry coil. This diagonal flux pipe region enhances the surface magnetic field (*B*) over the coil surface and improves the coupling coefficient to address misalignment. Also, this new geometry eliminates the power null phenomenon effect and limits power fluctuations in the WRIPT coupling architecture. The ferrite core in the coupler has a nonlinear magnetic field (*B*) on the surface, which is not easy to express and optimize using a conventional formula-based approach. Hence, the proposed ML-based ferrite core optimization of Δ–∇ pad finds its benefit in improving power transfer efficiency (PTE) by reducing power losses. This optimization method is applied to significant parameters (ferrite core position, number of cores, core layers, and core thickness) of the Δ–∇ geometry coil, by training 2.5% datasets out of the total possible cases. Also, the developed system was experimentally verified successfully and ensures that a Δ–∇ coupler achieves a higher PTE than the conventional geometry during various coupling conditions.**

***Index Terms*—Coil geometry, electric vehicle (EV) wireless charging, inductive coupler, interoperability, machine learning (ML), misalignment.**

I. Introduction

ELECTRIC vehicles (EVs) are the recent trending technology in the automobile industry to replace the functionality of fossil-fuel-operated internal combustion engine vehicles. The plugin cable insulation gets affected due to seasonal factors, and handling the bulky plugin charger for high-power applications is unsafe. These shortcomings of plugin charging methods are fulfilled by the wireless resonant inductive power transfer (WRIPT) charging system, by facilitating resonant inductive coupling between transmitter (Tx) and receiver (Rx) coils [1], [2]. The resonant compensator in the Tx and Rx coils of the WRIPT changing systems is extensively studied for effective coupling to enhance the power transfer efficiency (PTE) profile [5], [6], [7]. Meanwhile, different power converters are also studied for both static and dynamic charging WRIPT with their closed-loop control strategies [8], [9], [10], [11], [12]. A WRIPT inductive coupler inculcates coil winding, ferrite core, shielding, and coil holder; many research studies are focused on the coil geometrical structure [13], [14]. Various geometries studied in previous research investigations are comparatively discussed as per the charging types (static or in motion) in the review article [15]. Also, the comparison of the most widely adopted traditional WRIPT geometries is listed in Table I. Among all the geometries, double "D" or "DD" coil is mostly preferred for WRIPT application because of better misalignment tolerance. However, DD's drawback is the effect of the power null phenomenon (PNP) and its influence on power fluctuations during misalignment conditions. On the other side, the optimization of the coupler is necessary to obtain effective parameters, such

TABLE I
Comparison of Traditional Coil Geometries

Geometry	Pros	Cons
Flux Pipe [15]	Misalignment Tolerance High	Poor PTE, High Leakage Flux and Interoperability.
DD [15]	Good range of Misalignment Tolerance	Existing PNP effect, Power Fluctuations, Poor Interoperable, High Cross-coupling effect, Core optimization challenge.
DDQ [15]	Misalignment, Interoperable	Existing PNP Effect, Complex Decoupling, High Cross-coupling effect.
Bipolar [15]	Interoperable	Complex Decoupling Process
Other Conventional Coils [15]	Good range of Misalignment Tolerance	Poor PTE, Cross-coupling effect, Existing PNP effect, Power Fluctuations, Large Form Factor, High Thermal Loss.
Proposed Δ-∇ (Delta and Inverse Delta)	High Misalignment Coupling, Eliminating the PNP effect, Highly Interoperable, Reduced Leakage flux, simplified Decoupling construction and core location optimization.	However, this coupler has more manufacturing constraints.

Received 17 June 2024; revised 7 August 2024; accepted 14 September 2024. Date of publication 18 September 2024; date of current version 12 December 2024. This work was supported by Research Grant: Funding agency Department of Science and Technology (DST), Science and Engineering Research Board (SERB), Government of India, under core Research Grant, C.R.G./2020/004073. Recommended for publication by Associate Editor K. Park. *(Corresponding author: Narayanamoorthi R.)*

The authors are with the Department of Electrical and Electronics Engineering, SRM Institute of Science and Technology, Kattankulathur, Chennai 603203, India (e-mail: narayanr@srmist.edu.in).

Color versions of one or more figures in this article are available at https://doi.org/10.1109/TPEL.2024.3462980.

Digital Object Identifier 10.1109/TPEL.2024.3462980

as coupling coefficient, coupler outer dimension, number of coil turns, size, thickness of ferrite core, and shape of ferrite core [16]. In contrast with the coupler design, coil geometry and magnetic ferrite core optimization have not been extensively investigated in previous research studies. The impacts of using an optimally designed ferrite core for an inductive coupler and its methods are discussed [17], [18]. The coupling coefficient parameter optimization of the inductive coupler concerning ferrite core shape, size, layer, and thickness is investigated [16]. In [14] and [15], various ferrite core shapes are available per industrial coil design standards. The stepped-shape layered ferrite core proposed for well magnetic flux distribution is also investigated [19]. Numerous literature studies related to the design of ferrite cores have been investigated; the flat-type ferrite core that has the simplest construction and is preferred is studied [8], [13], [14], [15].

For designing a magnetic ferrite core, no formula-based theoretical designs are available because of its nonlinear magnetic field distribution property. The surface magnetic field "*B*" distribution according to the different shapes of the ferrite core is discussed [20], [21]. It is understood that the "*B*" distribution varies near the Tx and Rx coils based on the ferrite core shape for a specific geometry. Also, the nonlinear magnetic flux distribution property of the ferrite core affects the WRIPT coupler design parameters, such as coupling coefficient (K), surface magnetic flux density (B), self-inductance (L_s), and mutual inductance (L_m) at optimal locations of the ferrite core. The magnetic field distribution concerning the core location in the coupler is analyzed using empirical equations or simulation analysis [21], [22], [23]. However, the studies are limited to the known shape and structure of the coil that are not suitable for complex geometry. In most of the previous research, the couplers were designed using ferrite cores for higher coupling coefficients in trial-and-error-based simulation. However, this approach is not an accurate and time-consuming process to find the best performance of the coupler. In the meanwhile, the machine learning (ML)-based ferrite core optimization method for the coil is proposed for nonlinear systems [24]. Moreover, the ferrite-core-based structural optimization of the inductive pad to obtain higher coupling between Tx and Rx coils of the WRIPT charging system was experimented with a simulation-based data learning technique [25]. Also, this method applies to other types of inductive couplers to improve the coupling coefficient and PTE. However, the algorithm trained with only core location and other parameters of the coupler are not considered. In [26], the ML technique is proposed for learning the characteristics of the nonlinear nature of distributed magnetic fields produced in an inductive coupler concerning ferrite core position. However, there are only a limited number of existing research works on ML-based magnetic coupler optimization. Hence, considering the benefits and importance of magnetic ferrite core optimization, the optimal sizing, thickness, number of layers, and location of the ferrite core structure using ML algorithms are proposed in this article. The major contributions of this article are as follows.

1) This article presents a new delta and inverse delta (Δ–∇)-shaped wireless charging coupler that provides a diagonal flux pipe to enhance the surface magnetic field (B) and coupling coefficients during misalignment conditions.
2) It presents a Q-learning-based neural network (NN) ML algorithm to optimize the ferrite core position, number of core, core layers, and core thickness to develop an effective Inductive coupler.
3) The proposed system is validated in finite-element method (FEM) analysis and experimental testing for various coupling conditions.
4) The new Δ–∇ geometry coupler is comparatively discussed with the conventional DD geometry coil. The significant parameters, such as coupling coefficients, self-inductance, and mutual inductance, are investigated for various coupling conditions to ensure the effectiveness of the proposed coupler.

II. Delta And Inverse Delta (Δ-∇) Coupler

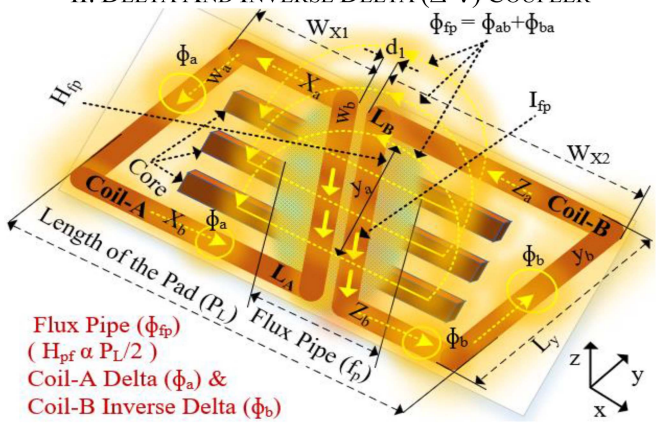

Fig. 1. Proposed Δ–∇ coil geometry.

II. Δ–∇ Coupler

The Δ–∇ coupler geometry is a combination of delta (Δ) and inverse delta (∇)-shaped inductive geometry coil arranged with an adjacent sequence. It introduces the advantage to the coupler with a high effective coupling coefficient because of the large overlapping flux region occurring due to the presence of a diagonal flux pipe (f_p). In this, coupling between the Tx and the Rx is enhanced with better offset lateral misalignment tolerance in the X-axis and intermediate air gap in the Z-axis. The ferrite core and the aluminum (Al) sheet under the coil force the flux to radiate on the one side of the pad to achieve higher surface flux ($H_{\rm fp}$ in the Z-axis) over the coil surface. The diagonal flux pipe in a coil will enhance the lateral misalignment tolerance to achieve high coupling in the intermediate air gap. Comparatively, this geometry reduces the number of litz wire strands for the design in the same power rating, as shown in Fig. 1

$$\emptyset_a = \frac{F_a}{R_{ab}}, \quad \emptyset_b = \frac{F_b}{R_{ab}}, \quad \emptyset_c = \frac{(F_{a+}F_b)}{(R_t||R_r)}. \tag{1}$$

The self and mutual magnetic field coupling for Δ–∇ geometry is represented by considering the coupling parameters and its coupling coefficients, along with the reluctance of coupling areas. $\Phi_{\rm fp}$ is the self-flux generated in the flux pipe region, and then, Φ_a and Φ_b are the self-flux generated from the coils A and B, respectively. The forces induced by the coils Δ–∇ are F_a and F_b, the self-reluctances of the coils A and B are R_t and R_r, and the mutual reluctance of the coils is R_{ab} in (1). The mutual links in the coupling region induce flux $\Phi_{\rm fp}$ from the flux pipe region and Φ_{ab} from coils A and B, as given in (2). Its reluctances

are R_{fp} and R_{ab}

$$\emptyset_{fp} = \frac{(F_{a+}F_{b})}{R_{fp}}, \quad \emptyset_{ab} = \frac{(F_{a+}F_{b})}{2R_{ab}} \tag{2}$$

$$L_{ab} = L_a + L_b + 2M \tag{3}$$

$$\left.\begin{array}{l} M = M_{waya} + M_{wayb} + M_{wbya} + M_{wbyb} \\ |M_{waya}| = \sum_{i=1}^{N}\sum_{j=i}^{N} M\left(l_{waya},\ d_{ij\_waya}\right) \\ |M_{wayb}| = \sum_{i=1}^{N}\sum_{j=i}^{N} M\left(l_{wayb},\ d_{ij\_wayb}\right) \\ |M_{wbyb}| = \sum_{i=1}^{N}\sum_{j=i}^{N} M\left(l_{wbyb},\ d_{ij\_wbyb}\right) \\ |M_{wbya}| = \sum_{i=1}^{N}\sum_{j=i}^{N} M\left(l_{wbya},\ d_{ij\_wbya}\right) \end{array}\right\} \tag{4}$$

$$\left.\begin{array}{l} l_{wayb} = l_{wbyb} = l_{wbya} = l_{waya} = L_y \_ d_{sp}\left(N-1\right) \\ d_{ij\_waya} = \left(j-1\right) d_{sp} + W_{X1} + d_1 \\ d_{ij\_wayb} = \left(j-i+1\right) d_{sp} + W_{X1} + W_{X2} \\ -\left(N-1\right) d_{SP} + d_1 \\ d_{ij\_wbya} = \left(j-i+1\right) d_{sp} + \left(N-1\right) d_{SP} + d_1 \\ d_{ij\_wbyb} = \left(j-i+1\right) d_{sp} + W_{X2} + d_1 \end{array}\right\}. \tag{5}$$

The inductance of the planner Δ–∇ geometry coil is given by (3). The self-inductance is (L_{ab}) with the cumulative inductance of the geometry coils A and B (L_a and L_b), and L_m is the mutual coupling inductance. The self-inductance of coil A is L_a. When coils A and B have the same geometry, $L_a = L_b$ is given

$$L_a = L_{wa} + L_{wb} + L_{Xa} + L_{Xb} + 2M_{wawb}2M_{XaXb} \tag{6}$$

$$\left.\begin{array}{l} |M_{wawb}| = \sum_{i=1}^{N}\sum_{j=i}^{N} M\left(l_{wawb},\ d_{ij\_wawb}\right) \\ |M_{XaXb}| = \sum_{i=1}^{N}\sum_{j=i}^{N} M\left(l_{XaXb},\ d_{ij\_XaXb}\right) \end{array}\right\} \tag{7}$$

$$\left.\begin{array}{l} l_{wa} = l_{Xa} = l_{wawb} = l_{waXb} = L_y - d_{sp}\left(N-1\right) \\ d_{ij\_wawb} = \left(j-1\right) d_{sp} + w_{X1} - \left(N-1\right) d_{sp} \\ d_{ij\_XaXb} = \left(j-1\right) d_{sp} + L_y - \left(N-1\right) d_{sp} \end{array}\right\} \tag{8}$$

$$\left.\begin{array}{l} L_{wa} = \sum_{i=1}^{N} L\left(r_0,\ l_{i_{wa}}\right) + \sum_{i=1}^{N}\sum_{j=i}^{N} M\left(l_{wa},\ d_{ij\_wa}\right) \\ l_{i\_wa} = L_y - \left(j-1\right) d_{sp} \\ d_{ij\_wa} = \left(j-1\right)\ d_{sp} \end{array}\right\}. \tag{9}$$

L_{xa} can be derived by replacing "*w*" with "*x*" in (9). The self-inductance of the coil after the influence of shielding material inductance used around the coil is given as

$$L_{\text{self}} = \frac{N\mu}{I}\int \overrightarrow{H}.dA. \tag{10}$$

The mutual inductance of the coil is identified by the induced voltage method at coupled conditions. The resultant inductive reactance of the coil (X_L) is represented by

$$X_L = \frac{\omega N\mu}{I}\int \overrightarrow{H}.dA. \tag{11}$$

The coupling factor (K) of the system is given by

$$K = \frac{\emptyset_{mfp} + \emptyset_{ab}}{\emptyset_{mfp} + \emptyset_m + \emptyset_a + \emptyset_b + \emptyset_{fp}}. \tag{12}$$

In this symmetrical geometrical coil, the established force is $F_1 = F_2$; then, coupling is given by

$$K = \frac{1/\left(\alpha_{ab} + \alpha_o\right)}{\emptyset_{mfp} + 0.5\alpha_{mab}}, \quad \alpha_o = \frac{1}{\left(R_t||R_r\right)}. \tag{13}$$

From (13), it is understood that the coupling coefficient depends on the optimal ferrite core placement. "*K*" increases by reducing ($\alpha_{\text{ab}} + \alpha_{\text{o}}$) and increasing ($\alpha_{\text{mfp}} + 0.5\alpha_{\text{mab}}$). The Steinmetz formula is used for the power loss calculation in ferrite core P_{fe} and volume integral over the core. Here, the Steinmetz parameters are k, α, and β, which all depend on the core material given in (14). The losses in Al are due to the eddy current effect, calculated by (15). Hence, it is necessary to reduce the P_{fe} and P_{al} losses in coupler optimization for the inductive coil. The optimal load resistance ($R_{\text{L,opt}}$) is for the equivalent ac resistance (R_{ac}); "$R_{\text{ac}\,R}$" is the equivalent ac resistance of the Rx coupler, and "$R_{\text{ac}\,T}$" is the equivalent ac resistance of the Tx coupler in the WRIPT coupling with a series–series capacitor compensator

$$P_{\text{fe}} = \iiint_V K f_o^{\alpha} B^{\beta} dv \tag{14}$$

$$P_{\text{al}} = \iint_A \frac{1}{2}\left(J_s.E^*\right) dA. \tag{15}$$

Then, the litz wire copper loss P_{cu} inculcates the ohmic dc loss P_{dc}, the skin effect loss in ac P_{skin}, and the proximity effect loss $P_{\text{prox,total}}$ which consists of total internal $P_{\text{prox,int}}$, and external $P_{\text{prox,ext}}$ proximity losses

$$R_{\text{ac}} = \frac{P_{\text{al}} + P_{\text{fe}} + P_{\text{cu}}}{I_{\text{rms}}^2} \tag{16}$$

$$R_{L,\text{opt}} = \omega M\sqrt{\frac{R_{\text{ac}R}}{R_{\text{ac}T}}} \tag{17}$$

$$P_{\text{dc}} + P_{\text{skin}} = n_{\text{str}}\, r_{\text{dc}} F_R\left(f_o\right)\left(\frac{I}{n_{\text{str}}}\right)^2 L_{\text{coil}} \tag{18}$$

$$\left.\begin{array}{l} P_{\text{prox,int}} = n_{\text{str}}\, r_{\text{dc}} G_R\left(f_o\right)\left(\frac{I^2}{2\pi^2 {d_a}^2}\right) L_{\text{coil}} \\ P_{\text{prox,ext}} = \sum_{i=1}^{N} n_{\text{str}} r_{\text{dc}} G_R\left(f_o\right) \int_{l_i} H_{\text{ext}}(l)^2 dl \end{array}\right\} \tag{19}$$

where n_{str} is the number of litz wire strands, r_{dc} is the dc resistance as per length of the litz wire, d_a is the diameter, H_{ext} is the external magnetic field in the coil surface, f_o is the operating frequency, and $F_R(f_o)$ and $G_R(f_o)$ are the frequency factors.

The PTE of the WRIPT system can be calculated as follows:

$$\eta = \frac{\omega_0^2 M^2 R_{L,\text{opt}}}{\left(R_{L,\text{opt}} + R_s\right)^2 R_s + M^2\omega_o^2\left(R_{L,\text{opt}} + R_s\right)} \tag{20}$$

where "η" is the efficiency, and "R_s" is the switching equivalent resistance and source resistance.

III. ML Optimization Technique

The ML-based coupler optimization technique involves a deep investigation of coupler design parameters, such as inductive coil geometry, ferrite core size, core thickness, number of core layers, core material, coupler outer dimension, and location/position of the ferrite core on the inductive coupler along with electromagnetic interference (EMI) shielding. The intermediate air gap between the surface Tx and Rx coils in the EV is maintained at 150 mm. In this research article, the proposed ML-based optimization algorithm concentrates on both the Rx and Tx couplers used in the WRIPT. The investigation that starts with Tx coil optimization to achieve a higher surface magnetic flux density (B) at the desired self-inductance (L_p) with optimal

design constraints benefits the reduced conductor length, weight, compact sizing with an optimal number of ferrite cores, positions, and thickness. Also, Tx inductive pad shielding is to reduce the risk of EMI radiation. Next, the Rx coupler is optimized for identical coupling (Δ–∇), followed by the optimization of the interoperable inductive coil with Double 'D' (DD) geometry in the Rx pick-up coupler to achieve maximum PTE. The mutual inductance *(L_m)* is the additional parameter considered for designing an optimal Rx coupler for an effective WRIPT coupling mechanism. The Tx and Rx coupler parameter variables are the considerable input datasets for the proposed algorithm. The optimal design of the Tx pad with the higher "*B*" value and the Rx pad for identical and interoperable geometry couplings is simultaneously tested for the effective coupling factor "*K*". The optimal coupling mechanism is achieved with the best selective location using a minimum number of cores out of the total possible core locations and a number of cores on the coupler for its outer dimension. By iterating for the minimum number of core position locations, it is seen that response influences the nonlinear distribution of "*B*" by various ferrite core location/position placements. The minimum number of datasets for nonlinear "*B*" distribution concerning core position location is analyzed successfully, and then, high "*K*" for core alignment can be obtained with ML algorithms. For predicting the nonlinear characteristics of "*K*" in the coupler based on ferrite core positions, the ML-based algorithm is much more suitable. To predict high "*K*" for a particular ferrite core position, the algorithm requires an accurate training process. To investigate the optimal number of core positions out of the total available 104 pieces, the coupler was implemented by iterating the ferrite cores in the *X*- and *Y*-axes to reduce and simplify the iterations. This optimization benefits by reducing the need for 104 ferrite cores, optimizing to 21 ferrite core positions, and achieving higher "*K*" with selected specific minimum numbers of pieces in optimal locations. The thickness optimization in core layers (height) was also performed before the selection of a specific core type. Hence, the effectiveness of the ML algorithm is applied in optimizing the number of cores, effective core positions, and thickness of ferrite core pieces, which will impact the performance in the coupling architecture. Therefore, the optimal coupler design in this article was achieved with reduced weight and cost by selecting the optimal core thickness, number of layers, and enhanced coupling factor "*K*".

A. *Proposed* Q-*Learning Algorithm*

Initially, learning and predicting the influence of the ferrite cores, which introduce a nonlinear function in "*B*" between couplers, are investigated using an ML-based supervised learning method. It requires more than a thousand of input-trained datasets; the input datasets are mined from the FEM analysis for each case, which is a time-consuming process for single input and outputs. Then, the number of ferrite core positions increases exponentially with the increase in the number of ferrite core pieces. Therefore, by considering the complexity of mining the number of datasets required for training the NN with limited datasets and the execution time, ML-based reinforcement learning can also learn the nonlinear system model function using the NN. It selects the possible actions performed by ferrite core positioning and rewards the optimal action through accurate prediction from trained datasets.

The *Q*-learning technique is one of the reinforcement learning algorithms; it rewards the output of the action from the environment when the agent raises the action inputs. Then, the reward

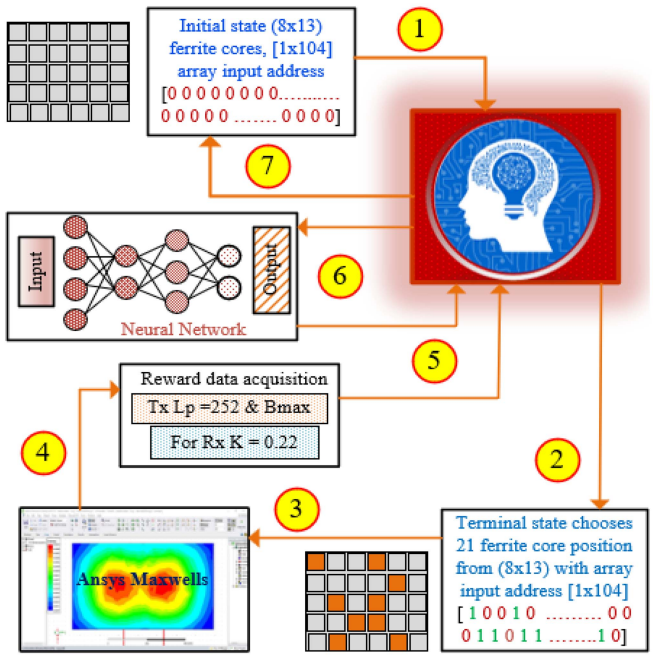

Fig. 2. Proposed *Q*-learning algorithm.

data are accumulated, and the agent chooses the upcoming action in the direction of maximizing the reward [27]. If the rewards are "*B*" for the Tx coil and "*K*" or mutual inductance "L_m" for the Rx coil of the *Q*-learning algorithm, the ferrite core position concerning rewards and its performance will be evaluated. This process is similar to the learning process in which an agent learns through *Q*-learning [28]. *Q*-learning was implemented through Python programming with the help of basic coding knowledge. Then, "*B*" for the Tx coil and "*K*" with "L_m" are obtained from the Ansys FEM analysis and the output rewards from the proposed *Q*-learning algorithm. The operating mechanism of the proposed ML-based *Q*-learning algorithm is shown in Fig. 2. At the initial state, agent actions are the input of the ferrite core present or air core region in the form of datasets. When *Q*-learning receives the input agent actions, it uses the decaying E-greedy policy to select the ferrite core positions randomly, which can maximize the coil performance optimally. The E-greedy policy that uses the core selection technique from our expectations is the random selection from the early episodes of the optimal learning process. The decay learning rate of the policy is given by

$$Q_t + 1\ (S_t, a_t) = Q_t\ (S_t, a_t) + \alpha(r_{t+1} + \gamma \max Q_t\,(S_{t+1}, a) - Q_t\,(S_t, a_t)\,. \tag{21}$$

The high "α" value depends on the *Q* value updated in the large range. The received reward outputs for the Tx coil are '*B*' and '*K*' at 'L_m,' are accumulated into the neural network, marking the completion of the learning process. The initial action of the process is optimal by a selection of 21 ferrite cores, and the remaining is air core in 104 positions using the E-greedy policy. The initial stage of action selection chooses 21 optimal ferrite cores as the terminal state input actions fed to the Ansys Maxwell environment. After the successful execution of the terminal state inputs to the environment return, a reward output is "*B*" for the Tx pad and "*K*" or "L_m" for the Rx from the coupler. Then, the rewards become an action nonlinear function (*Q* value), which

TABLE II
DESIGN PARAMETERS OF THE Q-LEARNING ALGORITHM

Design Parameter	Values
Total episodes	445
Learning rate	0.1
Exploration Initial	1.0
Exploration Final	0.3
Nodes of Hidden Layer 1	26
Nodes of Hidden Layer 2	26
Target network update period	3 episodes

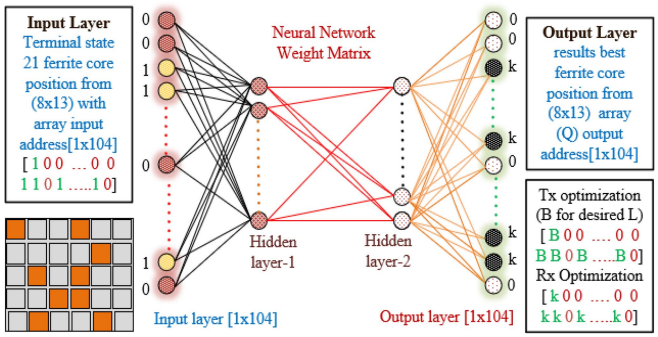

Fig. 3. Structure of the NN training method.

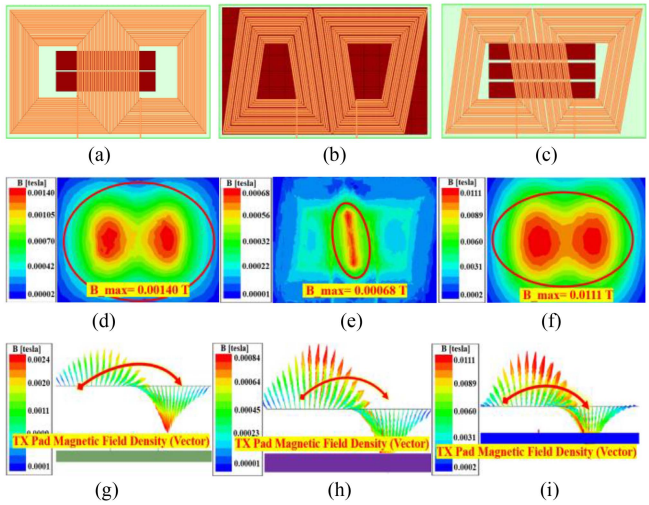

Fig. 4. Tx pad surface magnetic field (B) analysis. (a) DD geometry coil. (b) Δ–∇ geometry coil unoptimized. (c) Δ–∇ geometry coil optimized. (d) DD at $Z = 400$ mm. (e) Δ–∇ unoptimized at $Z = 400$ mm. (f) Δ–∇ optimized at $Z = 400$ mm. (g) DD coil vector representation. (h) Δ–∇ unoptimized coil vector representation. (i) Δ–∇ optimized coil vector representation.

is described as follows:

$$Tx: \; Q\left(s, a; \Theta^{-}\right) = B/L_P \tag{22}$$

$$Rx: \; Q\left(s, a; \Theta^{-}\right) = K/L_m \tag{23}$$

where θ^{-} is the main NN, "s" is the state, and "a" is the action in (22) and (23). The rewards for the Rx are "K" or "L_m" in (23), and the rewards for the Tx are (B) or Tx inductance (L_p) in (22). After the rewards are trained into the NN inputs, finally, the state is reset to the initial state, after the current episode ends. The proposed method was implemented with the help of an open-source platform [29]. The design parameters of Q-learning are listed in Table II.

B. Neural Networks

The input and output layers for processing the dataset with the NN model are shown in Fig. 3. The agent action input from the terminal stage, which selected optimal 21 core positions out of a total of 104, is used in the input layer as a [1 × 104] array with the information of the rewards earned. The output rewards for the agent input actions are represented with an output layer array after the prediction is tested with accuracy. The nodes in the input layers are connected to the hidden layer-1, and the hidden layer-2 nodes are connected to the output layer. Each node in this study has bias and weight for the simplest linear model.

In the NN training model, for both Tx and Rx optimization, the rewards of the output layers are either Tx "B" or Rx "K," so, generally, the output layer can be expressed with minimum node array. However, the implementation of 104 ferrite cores in the pads for optimization requires more node arrays to operate for various positions of ferrite cores. The NN performs the reverse terminal state operation to locate the input address for a suitable high-performance output. However, the NN was originally designed to operate in only a forward direction. Therefore, in this study, the output layers used for training the NN are designed for a [1 × 104] array with the information of rewards for agent actions, as shown in Fig. 4. This learning process is contributed to each ferrite core location in the array to separately analyze the optimal core location. After training the datasets by assigning the input layer arrays with all the nodes with weight one (which means the same ferrite core), the Q value in the output layer predicted by the NN-trained model for the corresponding core location and its reward output value can be shown. From the early trained datasets, the top 21 Q values by prediction, including the latest episode updates, are considered for a high probability of accuracy. The NN is conducted by selecting, taking the gradient descent to the loss functions in the following:

$$\text{Loss} = \left(Q\left(s, a; \Theta^{-}\right) - Q\left(s, a; \Theta^{-}\right)\right)^2 \tag{24}$$

where θ^{-} is the main NN and θ is the target NN. For every three episodes, the main network is updated, and the target network is updated identically. Also, the batch learning method is applied for network stability.

C. FEM Study

In this application, reinforcement learning is implemented with the constraint of a limited dataset, running on a system with the following specifications: Intel Core i7 11th Gen processor, 32 GB of RAM, and integrated ultra high definition (UHD) Graphics 750. The analyzing time per simulation for obtaining coupling parameters is approximately 10–15 min. Hence, the simulation was experimented with the Ansys scripting function provided in Maxwell, which runs fully automatically using Python. When terminal state input is fed to Ansys Maxwell environment for either Tx or Rx, FEM simulation is implemented and provides output L_m or K for the Rx coil and L_p or B for the Tx coil. All the FEM analyses in this article were performed

TABLE III
FEM ANALYSIS SIMULATION SETUP

Remarks		Simulation settings
Air gap		150 mm
Operating Frequency		85 kHz
Region (x, y, and z)		1:5:5
Permeability of CF295		$\mu_r = 3000 \pm 20\%$
Material	Windings	Copper
	Ferrite core	CF295
Solution Setup	no. of steps	10-time passes
	Error	0.1 %

using Ansys Maxwell EM21.1. The design parameters are listed in Table III.

IV. RESONANT INDUCTIVE COUPLER OPTIMIZATION

Significant parameters in the coupler that impact the PTE of the WRIPT systems are coil geometry, EMI shielding, number of ferrite cores, thickness of the core, number of core layers, selected ferrite core material, and optimal ferrite core position locations, which are the components that need to be investigated for coupler optimization. Coupler optimization enhances the PTE of the WRIPT coupling performance, with compact couplers that reduce the weight, cost, and quantity of materials needed for efficient coupler construction.

A. Comparisons of Coil Geometry

The coil geometry of DD, Δ–∇ (unoptimized), and Δ–∇ (optimized) coil surface magnetic field (*B*) performance is comparatively investigated using Ansys Maxwell's analysis. The investigation was conducted for various *Z*-axis alignments, including vector representations of geometry, as shown in Fig. 4. The geometrical coils are tightly wound to establish an effective "*B*" surface over the coil surface region. The designed DD geometry coil and its coupling performance for various *Z*-axis (distance between Tx and Rx coils is 400 mm) air gap and its vector representations are shown in Fig. 4(a), (d), and (g). The unoptimized Δ–∇ geometry coil with its surface magnetic field (*B*) performance is shown in Fig. 4(b), (e), and (h), and the optimized Δ–∇ geometry coil with its "*B*" is shown in Fig. 4(c), (f), and (i). Among all the designs, the optimized Δ–∇ geometry coil results in the highest surface magnetic field(*B*), followed by the optimized DD geometry coil in terms of performance. The unoptimized Δ–∇ geometry coil has a poor surface magnetic field "*B*" compared to DD and the optimized Δ–∇ geometry coil. Also, this unoptimized coupler needs more ferrite cores (104), which increase the weight of the coupler and power losses due to the heavy core material in the unoptimized system. The surface magnetic field (*B*) of the optimized Δ–∇ geometry coil offers a strong magnetic field for an air gap greater than half of the pad length ($H_{pf} > P_L/2$, as shown in Fig. 4(f) at a Z-axis air gap of 400 mm. Its comparative surface magnetic field (*B*) is illustrated in Figs. 4(d) and (e) for the unoptimized and optimized Δ–∇ geometry coil, respectively, with the vector representation shown in Figs. 4(e) and (f). This confirms that the proposed coupler achieves a high surface magnetic field (*B*) magnitude.

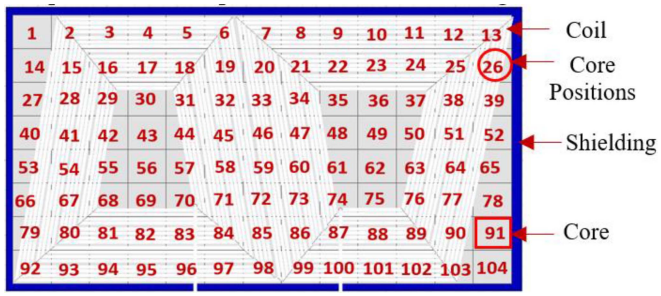

Fig. 5. Inductive coupler ferrite core position/location.

1) Shielding: For low- and medium-power applications, passive conductive and magnetic shielding has high human protection and low external interferences. It includes the shielding parameters of the ferrite core and the Al sheet. The distance between the Al sheet, coil, and ferrite core will introduce an effect of resonant capacitance that will highly affect "*B*" and coupler self-inductance. The leakage flux on the Al sheet introduces the eddy current power loss, which also affects the PTE. To develop optimal shielding for the coupler, the Tx and Rx coils with the Al sheet are experimented with air gap distance optimization [30], [31]. To perform coupler optimization using the FEM, the optimal distance is fixed for 0.2-mm air gap between the ferrite and Al sheet shielding. The designed Al sheet performs well in shielding the EMI and emitting the leakage flux into the intermediate air gap region.

2) Ferrite Position/Location: Since the WRIPT for EV application operates at a high operating frequency of 80–90 kHz. Here, high-frequency material is selected for the ferrite core to minimize the core losses. Based on the market availability of ferrite core material, "CF 295" was used for coupler design. This material has low power loss, has optimal temperature, has high permeability, is feasible for high-frequency operation, and is lightweight. The selected ferrite cores are positioned on top of Al shielding, and the geometrical coil is kept above the ferrite cores, as shown in Fig. 4(a)–(c). In the Tx pad, the coil is placed above the ferrite core, but vice versa for the Rx pad. The selected outer dimension (700 × 350 mm) of the pad requires a core array (8 × 13), in total 104 ferrite core pieces with a single core dimension size of about (9 × 55 × 45 mm); this same size is used for simulation and experimental tests. The construction arrangement of 104 ferrite cores with the proposed Δ–∇ geometrical inductive pad is shown in Fig. 5. Here, ferrite cores are placed in gray color and coil geometry in white color, and under the cores, the blue shielding plate is fixed. From this design, the effective "*K*" position concerning an optimal core and position location is investigated. The maximum number of cores for this desired coupler size (720 × 360 mm) that occupies a total of 104 cores is the maximum limit.

3) Coupler Optimization: Initially, the coupler is optimized to obtain maximum "*B*" in the pad's surface, for the desired self-inductance with an optimal number of ferrite cores and position location of the core. The ferrite core is placed below the coil geometry and above the shielding plate; here, the air cores are in gray color cubes, and maroon color cubes are the ferrite core material. To optimize the coupler with a minimum number of cores out of the total cores (104 cubes), the E-greedy policy is applied to find the optimal number of cores. It selects 21 cubes out of 104 cubes, which benefits in reducing the cost and

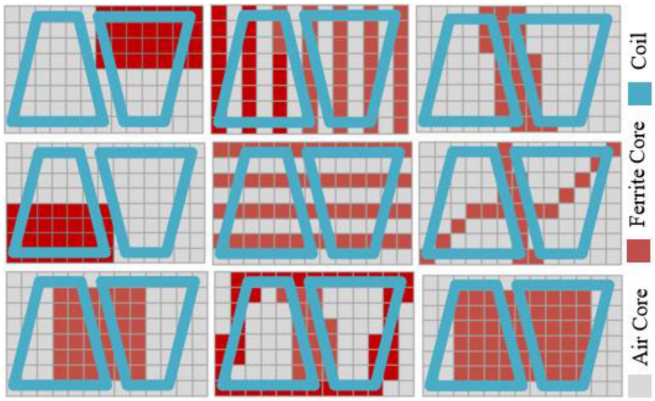

Fig. 6. Ferrite core position optimization logic.

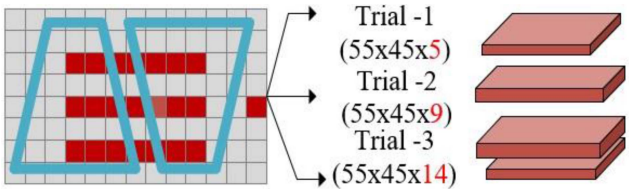

Fig. 7. Tx pad ferrite core thickness optimization.

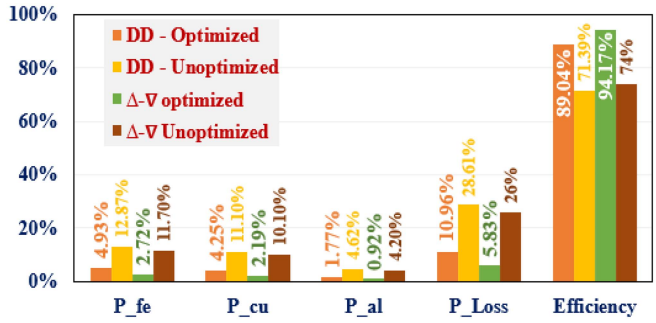

Fig. 8. Efficiency and power loss comparison for DD and Δ–∇ pads.

weight of more than 50% of the traditional coupler design. The selected cores with locations that depend on the earlier iteration results with high "*B*" are considered to build a core position optimization logic; some of the examples of logic combinations are shown in Fig. 6. From this investigation, the optimal logic of core position locations is framed as terminal state or agent action to the *Q*-learning algorithm. It provides the output rewards in the form of a surface magnetic field "*B*" value that is updated to the input datasets after three episodes. After Ansys analysis and NN training, it becomes an input dataset to improve the optimization process's predation accuracy.

By repeating the aforementioned logic with ferrite core position optimization simultaneously, core thickness is concentrated in the investigation to optimize the core performance. Optimizing the core thickness will reduce the core loss, weight, and cost of the coupler. Here, three different core sizes are considered for testing: $55 \times 45 \times 5$ mm, $55 \times 45 \times 9$ mm, and $55 \times 45 \times 14$ mm. The 14-mm thickness is analyzed with double-core layers on the z-axis with a combination of (5, 9 mm), and the optimal solution for the core is obtained to investigate the performance. As a result, the optimal ferrite position of this geometrical coil found near the flux path with 21 ferrite core cubes is arranged in combination, as shown in Fig. 7.

These optimization processes result in the DD coupler with 36 ferrite cores. It has an optimized location of two rows under the flux pipe region with two layers in each row. Each layer in a row has nine ferrite bars; for two layers with 18 ferrite bars and for two rows, all 36 ferrite cores are located in the designed optimal DD coupler. When it comes to the proposed Δ–∇ coupler geometrical coupler, three rows of one layer, each row with seven ferrite bars, are found with optimal location positions under the diagonal flux pipe region of the proposed Δ–∇ coupler. Comparatively, the proposed Δ–∇ coupler has reduced the number of cores required for the optimal coupler design, which benefits in several aspects. The core materials and the physical dimension of the core remain common for the entire coupler optimization process. The optimally designed coupler is converted into the equivalent circuit format, and ac high frequency is supplied to the coupler in the WRIPT system using Ansys Simplorer. This simulation analysis provides the data of the coupler, including various losses in the coupler. The design of the coupler is analyzed for the case of unoptimized and optimized couplings. This analysis is conducted for the traditional DD geometry and the proposed Δ–∇ geometry coupler and its outcomes in Fig. 8. Comparatively, the 9-mm thickness of the ferrite core has better optimal performance in coupler optimization; its surface "*B*" and vector magnitude are shown in Fig. 4(e), (f), (h), and (i). In Fig. 8, the Δ–∇ and DD geometry coil couplers are comparatively discussed for unoptimized and optimized pads. The efficiency and power loss are plotted for each coupler and coupler parameters, such as coil, Al, and core individually. Comparatively, the optimized Δ–∇ coupler has high efficiency and low power losses [32], [33]. Among all the parameters, the core loss is larger than coil and Al. The design and optimization of the coupler flowchart are shown in Fig. 9.

V. FEM Analysis of the Coupling Mechanism

After optimal coupler design, the effectiveness of the coupler is tested and investigated for identical and interoperable couplings using Ansys Maxwell's analysis. The results are plotted to ensure the effectiveness of the coupling mechanism. The parameters that impact the effectiveness of the coupler are self-inductance (L_s), mutual inductance (L_m), and coupling factor (K) for variations in the X-axis (lateral misalignment) and the Z-axis in intermediate air gap and are tested for various coupling mechanisms.

A. Identical Coupling Mechanism

In an identical coupling mechanism, the Tx and Rx pads have the same Δ–∇ geometry coil, with an intermediate air gap distance of 150 mm, as shown in Fig. 10. The Δ–∇ geometry coil optimization for the Tx coil is discussed in the previous section, and the Rx coil is optimized by changing the parameter variables of the coupler. The number of ferrite cores, position location placement, and thickness of the core are significant components concentrated for the Rx pad optimization of the coupler. The optimization logic of the ferrite core position is shown in Fig. 11(a)–(d). Here, the number of core positions increases with the increase in the number of cores. For a total of 104 cores, all the possible logics are 21 424, but, with the

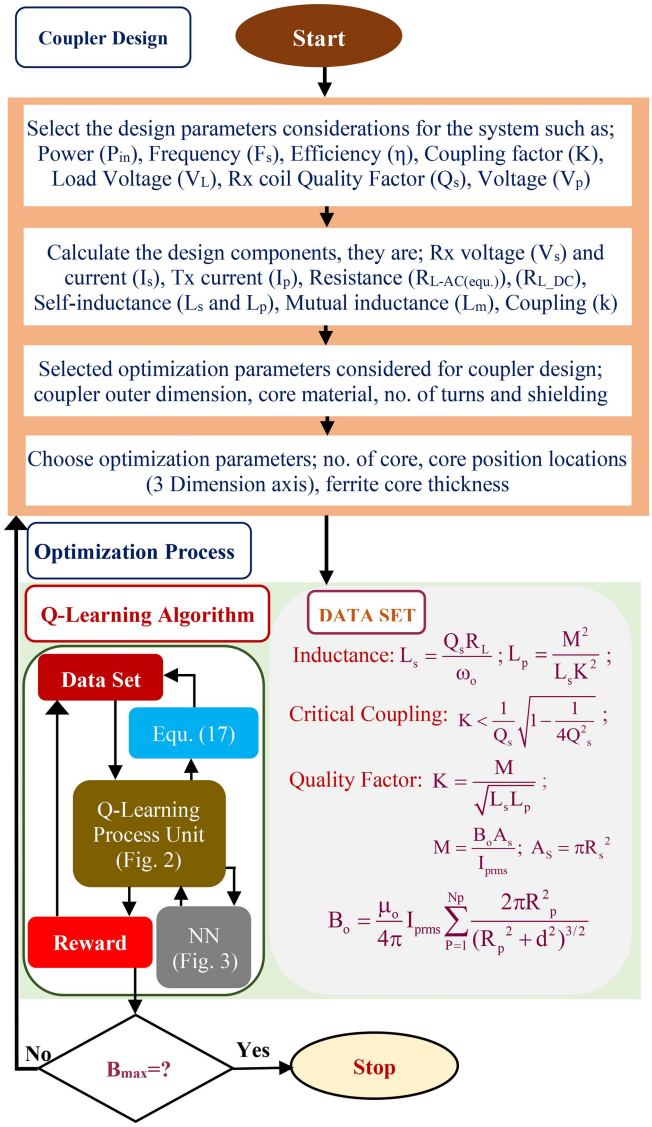

Fig. 9. Power pad design and the optimizing flowchart.

help of the E-greedy algorithm, the optimal number of cores is predicted around 21.

The optimal ferrite core positions are located with the help of the *Q*-learning algorithm through terminal state input agent action. After the process, it rewards "*K*" with a better "*B*" value for optimal core positions near the flux pipe, and its maximum surface "*B*" results are shown in Fig. 12. It is ensured that the coupling has a high "*K*" to achieve PTE in the WRIPT system. The performance of the coupler is analyzed for "*X*"-axis (lateral misalignment) and "*Z*"-axis (intermediate air gap) misalignments shown in Fig. 13. The misaligned coupling affects the PTE with the impact of decreases in L_m due to L_s changes in "*K*". Therefore, it is analyzed to ensure coupling effectiveness in this case.

The change in L_m that occurs due to variation in coupling coefficients "*K*" is affected concerning misalignment between the Tx and the Rx. Misalignment offset tolerance is analyzed for the ideal coupling case of the proposed, optimized Δ–∇ geometry coupler, as shown in Fig. 14. The analysis considers either the *Z*-axis for intermediate airgap variation or the *X*-axis

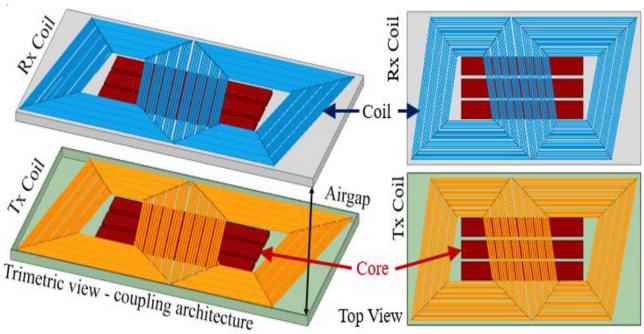

Fig. 10. Identical inductive coupling.

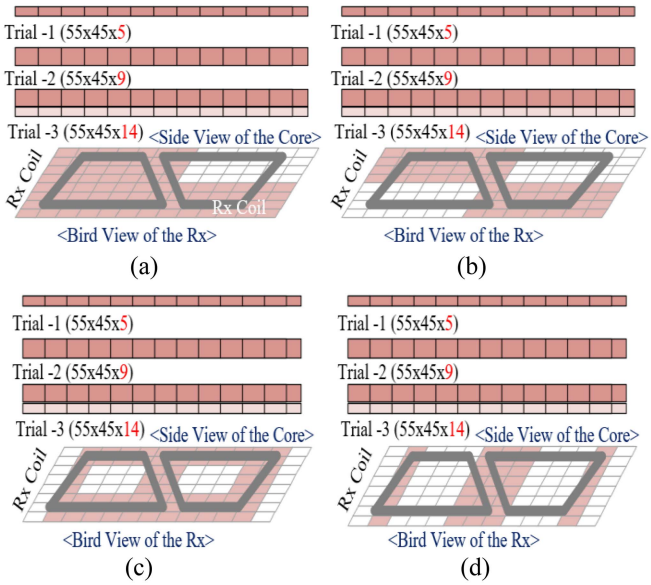

Fig. 11. Rx pad ferrite core optimization logic: a) Logic-A, b) Logic-B, c) Logic-C, and d) Logic-D.

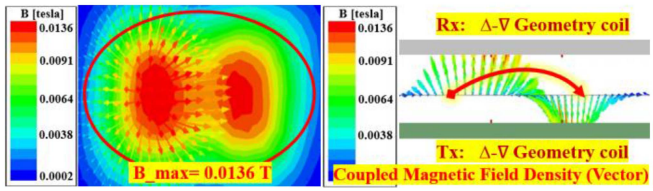

Fig. 12. Identical coupling surface "*B*" and its vector.

for lateral misalignment. It shows that an increase in lateral misalignment in the *X*-axis and intermediate air gap in the *Z*-axis will reduce the coupling factor (*K*).

B. Interoperable Coupling Mechanism

In this article, the DD geometrical Rx coil is selected for coupling analysis, as shown in Fig. 15. The optimization parameters of the DD coil are the number of cores, the position of the core, and the thickness of the core. Here, the core material and outer dimension of the coupler are considered constant. The proposed *Q*-learning algorithm obtains the optimal 16 ferrite cores near

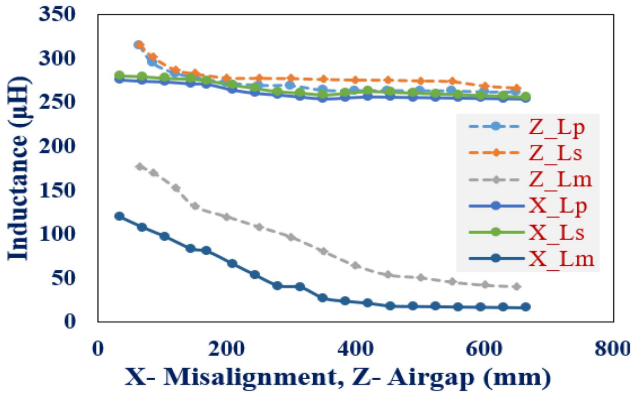

Fig. 13. Identical coupler performance.

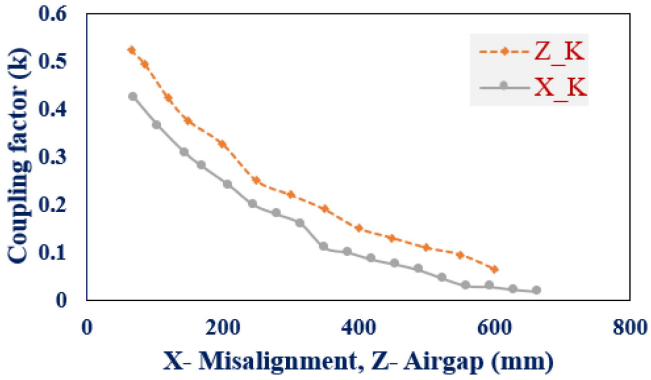

Fig. 14. Coupling factor for the identical coupler.

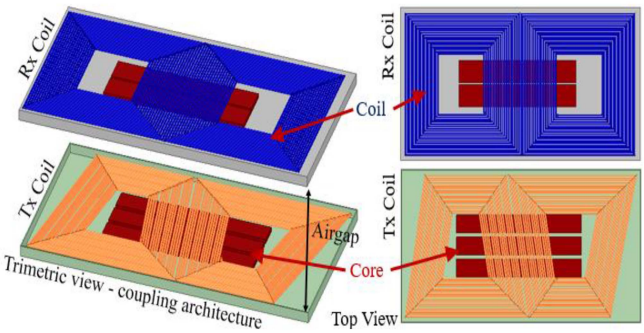

Fig. 15. Interoperable inductive coupling.

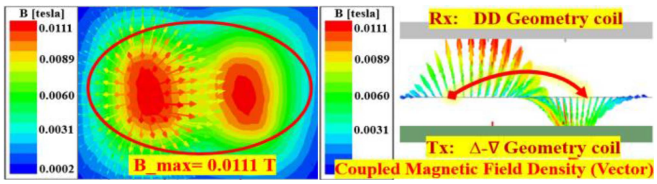

Fig. 16. Interoperable coupling surface "*B*" and the vector.

the flux pipe of the geometry, and it has a better high "*K*" between Tx and Rx coils. The surface "*B*" and its vector of the designed optimal interoperable coupling are shown in Fig. 16. It is ensured that the coupler mechanism has a highly effective coupling that links the Tx and Rx coils to achieve high PTE.

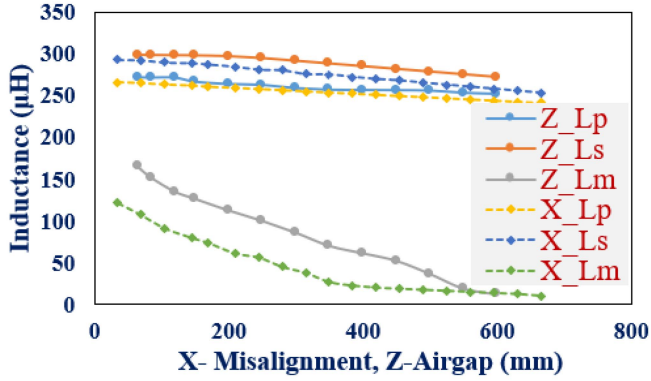

Fig. 17. Interoperable coupler performance.

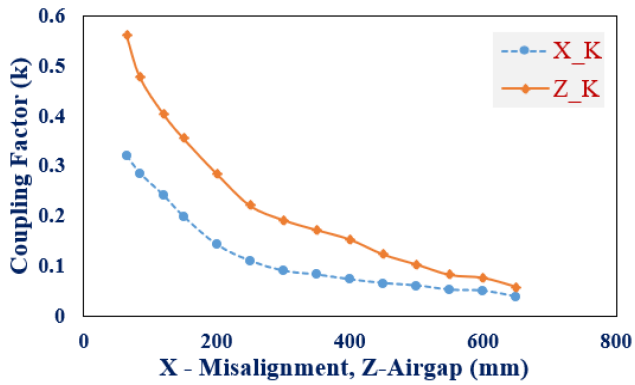

Fig. 18. Coupling factor for the interoperable coupler.

The proposed and optimized Δ–∇ geometry coil is coupled with a DD coil for analyzing the interoperable coupling performance. In this analysis, the Δ–∇ geometry coil is used as a Tx, and the DD coil is used in the Rx coupling architecture, with an intermediate 15-cm air gap. The performance of the interoperable coupler is analyzed for "*X*"'-axis (lateral misalignment) and "*Z*"-axis (intermediate air gap) alignments, and the obtained results of the inductance are shown in Fig. 17. The significant parameters *(L_p, L_s,* and *L_m)* of the coupler ensure that the effectiveness of the proposed coupler performs interoperability well in both the cases of analysis. The important parameter of PTE, the coupling factor, is affected due to misalignments tested for this case, as shown in Fig. 18. It comparatively ensures well interoperable operation along with identical coupling performance, in both the "*X*"-axis (lateral) and the "*Z*"-axis (intermediate air gap). The coupling factor that is heavily affected ($H_{\text{pf}} > P_L/2$) is ensured in Figs. 17 and 18.

VI. Experimental Validation

A. Experimental Setup

The traditional WRIPT system topology circuit is shown in Fig. 19. It consists of a high-frequency inverter with a source input (V_{in}), a primary capacitor (C_1), a wireless magnetic field coupling architecture with Tx and Rx coils (L_p and L_s), a secondary compensation capacitor (C_2), a rectifier, and load. The magnetic field coupling architecture is developed by optimally

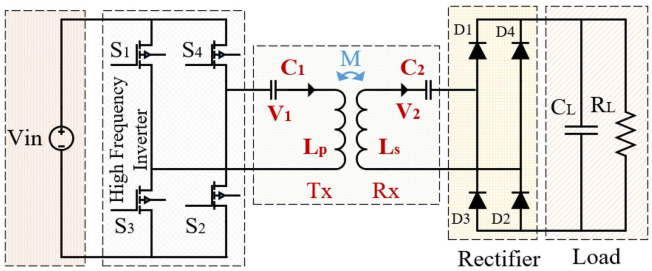

Fig. 19. Topology for experimental verification.

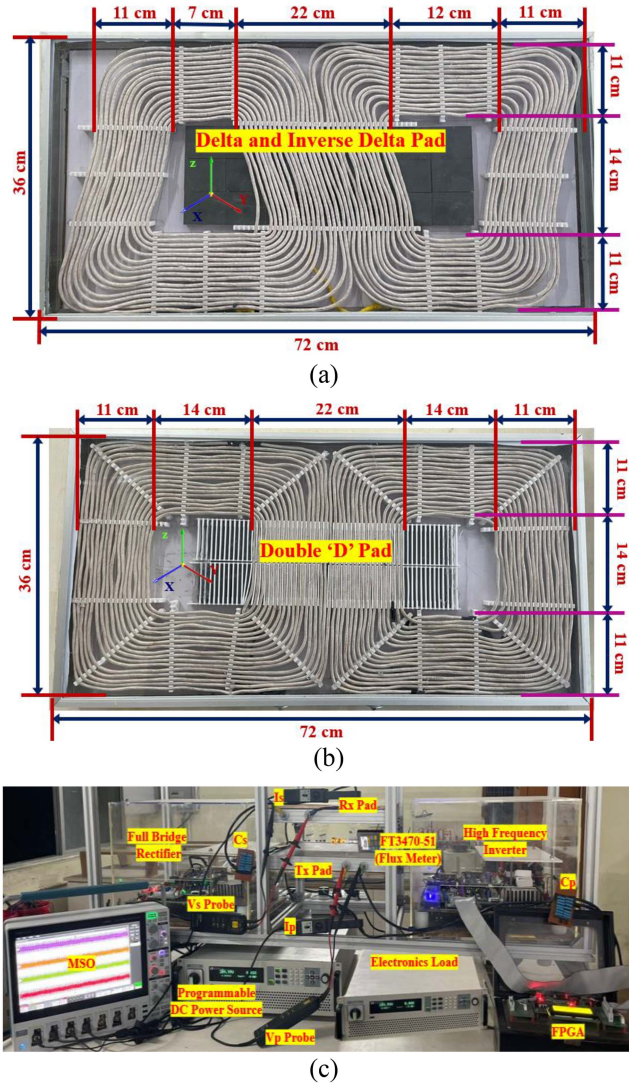

Fig. 20. (a) Proposed optimal Δ-∇ pad. (b) DD pad. (c) Hardware experimental model.

designing the new coupler using the ML optimization of coupler parameters, as shown in Fig. 20(b). The traditional DD geometry coil is shown in Fig. 20(a). The experimental setup is developed by considering the specifications in Table IV. The parameters are estimated for the WRIPT system power capacity. The developed hardware model is shown in Fig. 20(c); the identical and interoperable couplings are experimented with the proposed optimal Δ–∇ coil and traditional DD coil for interoperability analysis.

TABLE IV
EXPERIMENTAL DESIGN SPECIFICATION

Parameters	Specification
Power capacity (P_L)	3300 W
Frequency (f)	85000 Hz
Input Voltage (V_{in})	220 V
Airgap – Z-axis distance	150 mm
Calculated (Lp = Ls)	252 μH
Core Material	CF295
Litz wire (SWG 42) Strands	1050
Power pad outer diameter (mm)	700 x 350
Load Resistance (R_L)	27.312 Ω
Primary compensation capacitor	C_p = 37.35 nF
Secondary compensation capacitor	C_s = 37.5 nF

For coupling analysis, the couplers are designed for $L_p = L_s$. The inductive couplers are developed for fixed physical dimensions (720 × 360 mm), as shown in Fig. 20(a) and (b). The complete system is shown in Fig. 20(c). Hardware experimental model, which consists of WRIPT block models shown in Fig. 19. The system is equipped with the ITECH Programmable DC Power Supply (IT6012D-500-80) source and the ITECH Regenerative Power System (IT6005B-80-150) used as an electronic load. The Tx pad is energized with the high-frequency inverter through a series compensation (C_p) capacitor, and it is controlled through Spartan 6 field-programmable gate array. The Rx pad is fixed above the Tx pad with an intermediate air gap of around 150 mm; it picks up the Tx power and supplies it to the full-bridge rectifier through a secondary series compensation capacitor (C_s). The six-channel mixed signal oscilloscopes (MSO) is used to measure the current and voltage signal of the WRIPT system. The flux meter FT 3470-51 is used to measure the flux density of the inductive coupler for experimental analysis.

B. Experimental Results

The magnetic flux density (B) of the coupler is measured for a 3-D axis moment above the coupler surface. The 3-D axes are Y-axis, X-axis, and Z-axis, which are shown in Fig. 21(a)–(c), respectively. It represents the surface magnetic flux around the coupler for physical dimension 720 × 360 mm above the coupler surface. The comparative results are plotted for the DD coupler in dotted lines and the proposed Δ–∇ in line format for the 3-D axis (X, Y, and Z), and its resultant magnitude is in the plots. Its results are the resultant of DD that is dominated by the constant flux of the Δ–∇ coupler.

The 3-D axis (X, Y, and Z) moments of the flux meter probe (FT 3470-51) are plotted individually, and its results are the resultant sum of the 3-D axis moment flux magnitude. In Fig. 21(a), the magnetic flux density surface analysis in the 3-D axis and its resultant are fluctuating (270–410 mm) within the coupler undergoing low flux magnitude. This drawback is overcome by the proposed Δ–∇ coupler, which has a constant magnetic flux density throughout the coupler surface region. In Fig. 21(b), the magnetic flux density surface analysis in the 3-D axis and its resultant are limited for distance (0–60 mm and 300–360 mm) around the coupler; this can be addressed with the Δ–∇ coupler, and a constant flux magnitude is achieved. In Fig. 21(c), the magnetic flux density surface analysis in the 3D axis and its resultant are limited and undergo fluctuation in

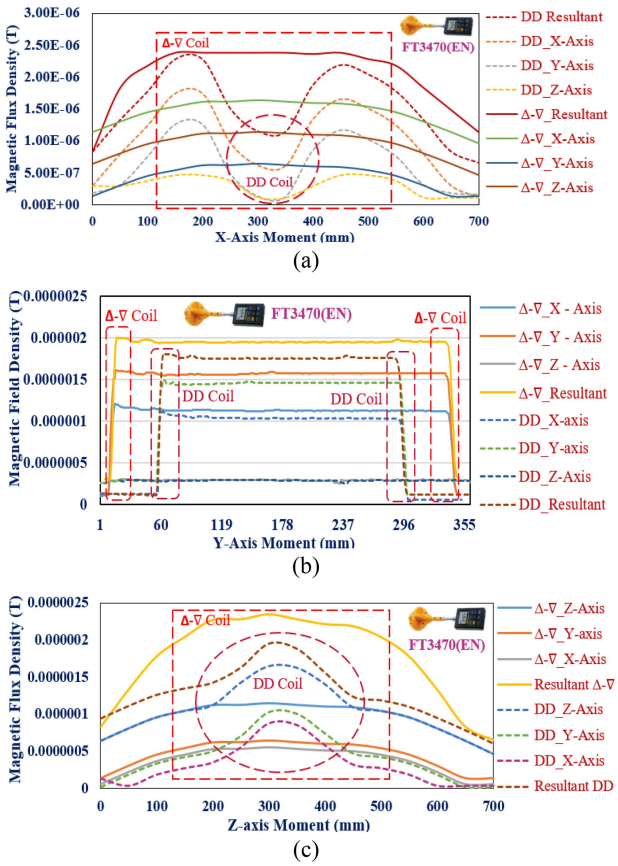

Fig. 21. (a) Magnetic flux density surface analysis in the *y*-axis. (b) Magnetic flux density surface analysis in the *x*-axis. (c) Magnetic flux density surface analysis in the *z*-axis.

duration (240–440 mm); this can be addressed with the Δ–∇ coupler and a constant peak magnitude is achieved. The results of the resultant magnitude of the Δ–∇ coupler ensure that the effectiveness of coupling strength achieves higher magnetic field around the coupler enhances coupling coefficients, limits leakage flux, and reduces the fluctuations. It undergoes high misalignment tolerance coupling and good interoperable coupling. The WRIPT system magnetic field coupling has experimented with the identical coupling of the proposed Δ–∇ coil and then the DD coil in both the Tx and the Rx. Then, interoperability is ensured by experimenting with the Δ–∇ Tx coil and the DD coil in the Rx. The test results are plotted in the graph given in Fig. 22, which shows that the increase in power capacity will increase efficiency to achieve maximum PTE at the resonant frequency.

This plot shows the comparative results obtained from the investigation, and it ensures that the proposed Δ–∇ performs well at the rated power capacity compared to the DD coil. Also, it ensures PTE for identical and interoperable couplings.

Then, the coupler is experimented by introducing variation in the "*X*"-axis and the "*Z*"-axis (air gap) for both the identical and interoperable couplings of the proposed Δ–∇ coil and the DD coil. Then, the power capacity for misalignment is plotted, which shows that increase in misalignment will reduce the power capacity. In this case, the optimized Δ–∇ coil performs better than the DD coil, which is comparatively ensured in the plot

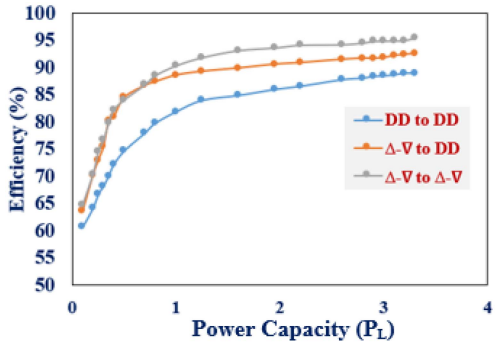

Fig. 22. Experimental result at well-aligned coupling.

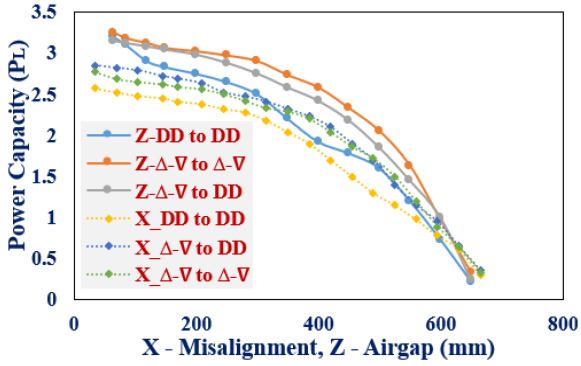

Fig. 23. Experimental result power capacity (P_L) versus misalignment coupling.

TABLE V
EXPERIMENTAL RESULTS

Coupling	Coupler	Efficiency	Power & Frequency
Identical	DD - DD	89.04 %	
Identical	Δ-∇ – Δ-∇	96.17 %	3.3 kW & 85
Interoperable	Δ-∇- DD	95.63 %	KHz

shown in Fig. 23. In the well-aligned case, the experimental results with the Tx coil voltage (V_1), current (I_2) and Rx coil voltage (V_2), current (I_2) for identical coupling of the proposed Δ–∇ coil and the DD coil are shown in Fig. 24(a) and (c). Then, the interoperable coupling of DD and Δ–∇ is shown in Fig. 24(b). V_{in} supplied by the source and the PTE was measured by varying the load resistance to the rated power capacity with a 15-cm intermediate air gap, as listed in Table V. The efficiency increases with the increase near the rated power capacity, and the proposed coupler system efficiency achieves 5.12% higher than that of the DD coupler for 3.3-kW rated power. The power fluctuation is eliminated in the Δ–∇ coupler, as shown in Fig. 24(a) and (b). It is ensured that the proposed Δ–∇ coupler eliminates the PNP effect and achieves the desired power transfer profile in the coupling. This is obtained by developing an optimal pad for the proposed new geometry coil with a large diagonal flux pipe region in the coupler geometry for the WRIPT system. Also, it is ensured that the coupler is better suitable for high misalignment tolerance, and coupling is highly interoperable.

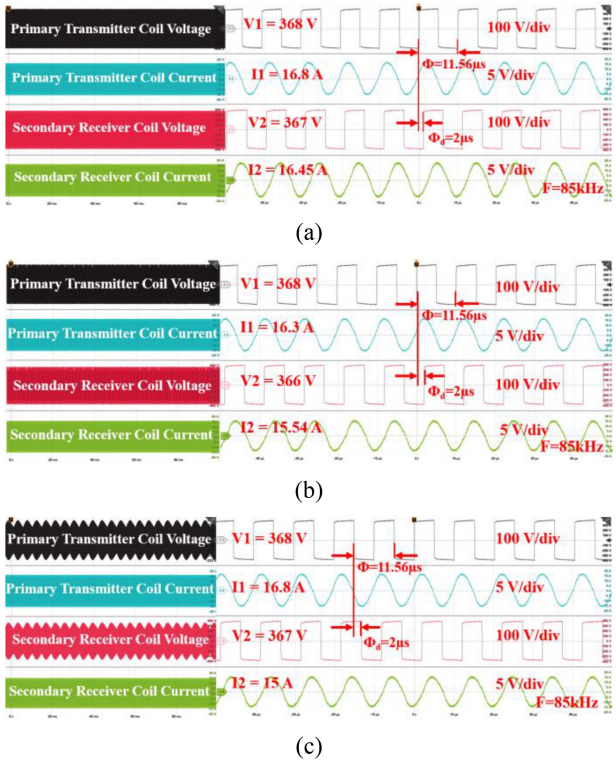

Fig. 24. Couplings. (a) Identical proposed Δ–∇ to Δ–∇. (b) Interoperable DD to Δ–∇. (c) Identical traditional DD to DD.

VII. Conclusion

In this article, a Δ–∇ geometry coil for WRIPT is proposed and optimized to develop an effective coupler using an ML-based reinforcement algorithm with NN combination and is demonstrated successfully. This optimization benefits the development of an optimal pad with an effective positioning of ferrite cores, number of cores, and thickness of ferrite cores. The new geometry coil has good coupling features in the *X*-axis (lateral misalignment) and *Z*-axis (intermediate air gap) with better coupling coefficients; it eliminates the PNP effect for various misalignments. This combined Δ–∇ coil structure has a flux-overlapping region, which enhances the surface magnetic field (*B*) and effectively couples with the Rx coil. Comparatively, the Δ–∇ coil demonstrates better coupling features than the DD coil studied. Also, it has highly interoperable performance with 5.12% of the DD Rx coil experimented with 7.12% in identical Δ–∇ coupling. The 3.3-kW power capacity experimental results ensure the effectiveness of coupler performance with high PTE during identical and interoperable couplings with various conditions of misalignments. It is ensured that the coupling effectiveness eliminates the PNP effect, power fluctuations, and high misalignment tolerance coupling. This optimization technique is possible for a wider range of coupler designs for the WRIPT system for future creative works.

References

[1] X. Hao et al., "Light-duty plug-in electric vehicles in China: Evolution, competition, and outlook," SAE Tech. Paper 2023-01-0891, 2023.

[2] O. C. Onar, J. M. Miller, S. L. Campbell, C. Coomer, C. P. White, and L. E. Seiber, "A novel wireless power transfer for in-motion EV/PHEV charging," in *Proc. 28th Annu. IEEE Appl. Power Electron. Conf. Expo.*, 2013, pp. 3073–3080.

[3] J. M. Miller, P. T. Jones, J.-M. Li, and O. C. Onar, "ORNL experience and challenges facing dynamic wireless power charging of EVs," *IEEE Circuits Syst. Mag.*, vol. 15, no. 2, pp. 40–53, Second Quarter 2015.

[4] A. Foote, O. C. Onar, S. Debnath, J. Pries, V. P. Galigekere, and B. Ozpineci, "System design of dynamic wireless power transfer for automated highways," in *Proc. IEEE Transp. Electrific. Conf. Expo*, 2019, pp. 1–5.

[5] X. Wang, S. Zhao, Z. Yang, Y. Liu, H. A. Mantooth, and L. Ding, "Comprehensive analysis of synchronous rectifying signal delay of high-frequency LLC resonant DC/DC converter," *IEEE Trans. Power Electron.*, vol. 39, no. 10, pp. 13348–13364, Oct. 2024, doi: 10.1109/TPEL.2024.3414595.

[6] M. Venkatesan et al., "A review of compensation topologies and control techniques of bidirectional wireless power transfer systems for electric vehicle applications," *Energies*, vol. 15, no. 20, 2022, Art. no. 7816.

[7] U. D. Kavimandan, V. P. Galigekere, O. Onar, M. Mohammad, B. Ozpineci, and S. M. Mahajan, "The sensitivity analysis of coil misalignment for a 200-kW dynamic wireless power transfer system with an LCC-S and LCC-P compensation," in *Proc. IEEE Transp. Electrific. Conf. Expo*, 2021, pp. 1–8.

[8] Y. Shanmugam et al., "A systematic review of dynamic wireless charging system for electric transportation," *IEEE Access*, vol. 10, pp. 133617–133642, 2022.

[9] X. Li et al., "A high-efficiency IPT system with series-capacitor full-bridge configuration and inverse coupled current doubler rectifier for high input, low voltage and high output current applications," *IEEE Trans. Power Electron.*, vol. 39, no. 9, pp. 11849–11861, Sep. 2024, doi: 10.1109/TPEL.2024.3414416.

[10] V. Ramakrishnan et al., "A comprehensive review on efficiency enhancement of wireless charging system for an electric vehicles application," *IEEE Access*, vol. 12, pp. 46967–46994, 2024.

[11] Y. Shanmugam and R. Narayanamoorthi, "Receiver side-controlled load-independent S-LCC/SP-compensated multileg inverter-powered dynamic charging system," *IEEE Trans. Ind. Electron.*, 2024.

[12] M. Venkatesan, R. Narayanamoorthi, A. Emara, and Y. Y. Ghadi, "Fuzzy logic controlled pulse density modulation technique for bidirectional inductive power transfer systems," *IEEE Access*, vol. 12, pp. 55184–55200, 2024.

[13] F. Y. Lin, G. A. Covic, and J. T. Boys, "Evaluation of magnetic pad sizes and topologies for electric vehicle charging," *IEEE Trans. Power Electron.*, vol. 30, no. 11, pp. 6391–6407, Nov. 2015.

[14] D. Patil, M. K. McDonough, J. M. Miller, B. Fahimi, and P. T. Balsara, "Wireless power transfer for vehicular applications: Overview and challenges," *IEEE Trans. Transp. Electrific.*, vol. 4, no. 1, pp. 3–37, Mar. 2018.

[15] J. Rahulkumar et al., "An empirical survey on wireless inductive power pad and resonant magnetic field coupling for in-motion EV charging system," *IEEE Access*, vol. 11, pp. 4660–4693, 2023.

[16] W. Zhang, J. C. White, A. M. Abraham, and C. C. Mi, "Loosely coupled transformer structure and interoperability study for EV wireless charging systems," *IEEE Trans. Power Electron.*, vol. 30, no. 11, pp. 6356–6367, Nov. 2015.

[17] A. D. Scher, M. Mohammad, B. Ozpineci, and O. Onar, "Design and optimization of cancellation coil topologies for a ferrite-less wireless EV charging pad," in *Proc. IEEE Transp. Electrific. Conf. Expo*, 2021, pp. 1–7.

[18] M. Budhia, G. A. Covic, and J. T. Boys, "Design and optimization of circular magnetic structures for lumped inductive power transfer systems," *IEEE Trans. Power Electron.*, vol. 26, no. 11, pp. 3096–3108, Nov. 2011.

[19] C. Park, S. Lee, G.-H. Choi, and C. T. Rim, "Innovative 5-m-off distance inductive power transfer systems with optimally shaped dipole coils," *IEEE Trans. Power Electron.*, vol. 30, no. 2, pp. 817–827, Feb. 2015.

[20] G. A. J. Elliott, G. A. Covic, D. Kacprzak, and J. T. Boys, "A new concept: Asymmetrical pick-ups for inductively coupled power transfer monorail systems," *IEEE Trans. Magn.*, vol. 42, no. 10, pp. 3389–3391, Oct. 2006.

[21] M. Kacki, M. S. Rylko, J. G. Hayes, and C. R. Sullivan, "A study of flux distribution and impedance in solid and laminar ferrite cores," in *Proc. IEEE Appl. Power Electron. Conf. Expo.*, 2019, pp. 2681–2687.

[22] M. Wang, J. Feng, Y. Shi, and M. Shen, "Demagnetization weakening and magnetic field concentration with ferrite core characterization for efficient wireless power transfer," *IEEE Trans. Ind. Electron.*, vol. 66, no. 3, pp. 1842–1851, Mar. 2019.

[23] F. Marketos, D. Marnay, and T. Ngnegueu, "Experimental and numerical investigation of flux density distribution in the individual packets of a 100 kVA transformer core," *IEEE Trans. Magn.*, vol. 48, no. 4, pp. 1677–1680, Apr. 2012.

[24] K. Na, J. Kim, and Y.-J. Park, "Machine learning-based power control technique for wireless power transfer," in *Proc. IEEE Wireless Power Transfer Conf.*, 2020, pp. 443–446, doi: 10.1109/WPTC48563.2020.9295544.

[25] B.-G. Choi and Y.-S. Kim, "New structure design of ferrite cores for wireless electric vehicle charging by machine learning," *IEEE Trans. Ind. Electron.*, vol. 68, no. 12, pp. 12162–12172, Dec. 2021.
[26] B.-G. Choi, E. S. Lee, and Y.-S. Kim, "Optimal structure design of ferromagnetic cores in wireless power transfer by reinforcement learning," *IEEE Access*, vol. 8, pp. 179295–179306, 2020.
[27] V. Mnih et al., "Playing Atari with deep reinforcement learning," in *Proc. NIPS Deep Learn. Workshop*, 2013, pp. 1–9.
[28] "Deep reinforcement learning," Accessed: 18 Jul. 2023. [Online]. Available: https://deepmind.com/blog/deepreinforcement-learning
[29] "Human-level control through deep reinforcement learning," Accessed: Jul. 24, 2023. [Online]. Available: https://sites.google.com/a/deepmind.com/dqn/
[30] P. L. Sergeant, L. R. Dupre, M. De Wulf, and J. A. A. Melkebeek, "Optimizing active and passive magnetic shields in induction heating by a genetic algorithm," *IEEE Trans. Magn.*, vol. 39, no. 6, pp. 3486–3496, Nov. 2003.
[31] P. Deng, C. Tang, M. Sun, Z. Liu, H. Hu, and T. Lin, "EMI suppression method for LCC-S MC-WPT systems by parameter optimization," *IEEE Trans. Power Electron.*, vol. 39, no. 9, pp. 11134–11147, Sep. 2024, doi: 10.1109/TPEL.2024.3414343.
[32] Z. Li, X. Li, Y. Zhou, Y. Liu, and M. Ban, "Improving misalignment tolerance for the wireless charging system using multiple coils coupler," *IEEE Trans. Power Electron.*, vol. 39, no. 6, pp. 7721–7735, Jun. 2024.
[33] G. Zhu, J. Dong, G. Yu, W. Shi, C. Riekerk, and P. Bauer, "Optimal multivariable control for wide output regulation and full-range efficiency optimization in LCC-LCC compensated wireless power transfer systems," *IEEE Trans. Power Electron.*, vol. 39, no. 9, pp. 11834–11848, Sep. 2024, doi: 10.1109/TPEL.2024.3414157.

Rahulkumar J received the B.Eng. degree in electrical and electronics from the St.Joseph's Institute of Technology, Chennai, India, in 2015, and the M.Eng. degree in power electronics and drives from the Government College of Technology, Coimbatore, India, in 2019. He is currently working toward the Ph.D. degree with the Department of Electrical and Electronics Engineering, SRM Institute of Science and Technology, Chennai, India.

He is a Senior Research Fellow with the Department of Electrical and Electronics Engineering, SRM Institute of Science and Technology. His research interests include electric vehicles, power electronics, data acquisition systems, embedded systems, and wireless power transfer for electric vehicle charging.

Narayanamoorthi R (Member, IEEE) received the bachelor's degree in electrical engineering and the master's degree in control and instrumentation from Anna University, Chennai, India, in 2009 and 2011, respectively, and the Ph.D. degree in wireless power transfer from the SRM Institute of Science and Technology, Chennai, in 2019.

He is currently an Associate Professor with the Department of Electrical and Electronics Engineering, SRM Institute of Science and Technology. His research interests include wireless power transfer, electric vehicles, power electronics, artificial intelligence, machine learning in renewable energy systems, and embedded systems for smart sensors.